Int J Adv Manuf Technol (2014) 71:1949–1959
DOI 10.1007/s00170-014-5627-8

ORIGINAL ARTICLE

Thermal analysis of the hydrostatic spindle system by the finite volume element method

Hao Su · Lihua Lu · Yingchun Liang · Qiang Zhang · Yazhou Sun

Received: 17 September 2013 / Accepted: 13 January 2014 / Published online: 28 January 2014

Abstract The temperature rise of an ultra-precision machine tool has a great impact on machining accuracy. Meanwhile, the hydrostatic spindle system is the main internal heat source of the machine tool, which consists of a hydrostatic spindle and a direct current motor. Therefore, it is very significant to study the thermal behaviors of the hydrostatic spindle system. In this paper, an integrated heat-fluid–solid coupling model of the hydrostatic spindle system is built to simulate the heat generation process and the fluid–structure conjugate heat transfer. Then a finite volume element method (FVEM) is proposed by combining the advantages of the finite volume method (FVM) and the finite element method (FEM) with consideration of the interaction of the temperature field, thermal deformation, and eccentricity. Based on the proposed model and method, the thermal characteristics of the hydrostatic spindle system are studied by the two-way heat-fluid–solid coupling analysis. The temperature variations obtained by the simulation agree well with the experimental results, which validate the proposed model and method.

Keywords Hydrostatic spindle system · Heat-fluid–solid coupling model · Finite volume element method · Thermal behavior

1 Introduction

The thermal error caused by the internal and external heat sources of machine tools accounts for more than 50 % of the overall geometrical inaccuracies of workpieces [1, 2]. Therefore, the thermal characteristics of machine tools have been widely studied in order to improve the machining precision [3]. Meanwhile, the spindle system, which consists of the spindle and the motor used in the ultra-precision machine tool, is the main internal heat source and has been widely studied [4, 5].

Because thermoelastic deformation processes of machine tools are so complicated, the finite element method (FEM) has been used as the major method to study them [6]. Chen et al. studied the effects of thermal deformation on oil film thickness, stiffness, load capacity, and machining accuracy of a hydrostatic spindle by proposing a thermomechanical error model [7]. Zhao et al. simulated the temperature field and the thermal error of a spindle by the finite element method and studied the changes of the temperature and the thermal error with time [8]. Zhang et al. proposed a whole machine temperature field and thermal deformation modeling and simulated the thermal behaviors of the vertical machining centers by the thermal-structure coupling method [9]. However, in the above researches, the heating sources were just simplified to constant values (temperatures or heat generation rates) obtained by the theoretical equations, which reduced the calculation accuracy. Mayr et al. proposed a finite difference element method (FDEM) by combining the advantages of the finite difference method (FDM) and the finite element method (FEM) in a way of sequential coupling and built a compensation model of a machine tool based on the proposed method [10, 11]. Jedrzejewski et al. proposed a hybrid high-speed machining center headstock model based on the finite element method and the finite difference method in order to guide the design of machine tools [12]. Holkup et al. proposed a thermomechanical model of the spindle based on the finite element method to predict the temperature distribution and the thermal deformation [13]. Li et al. improved the accuracy of the thermal simulation of a spindle system by considering the influence of the thermal contact resistances and the convective heat transfer coefficients [14]. However, the interaction

H. Su · L. Lu (✉) · Y. Liang · Q. Zhang · Y. Sun
Center for Precision Engineering, Harbin Institute of Technology,
P.O. Box 413, Harbin, Heilongjiang 150001,
People's Republic of China
e-mail: 11B908036@hit.edu.cn

between the temperature rise and the thermal deformation was not considered in the methods and the models proposed above. Therefore, Mayr et al. suggested that the more accurate simulation model and calculation method should be proposed in the thermal analysis of the machine tools [15].

This paper proposes an integrated heat-fluid–solid coupling model of the hydrostatic spindle system. The heat generation process is simulated directly by the proposed model, and the fluid–structure conjugate heat transfer is also included in the model. So the temperature field is calculated more accurately. Meanwhile, in order to consider the interaction among temperature rise, thermal deformation, and eccentricity, a finite volume element method (FVEM) is proposed. Based on the integrated model and the FVEM, the influence of temperature rise on the performance of the hydrostatic spindle system is studied by the two-way heat-fluid–solid coupling analysis. Finally, the experiment is set up to validate the proposed model and method.

2 Structure of the hydrostatic spindle system

The structure of the studied hydrostatic spindle system of a fly cutting machine tool is shown in Fig. 1. Surfaces (1)–(4) in Fig. 1 denote the different surfaces with different heat transfer regimes used in Section 4.

For the studied hydrostatic spindle system, the spindle is driven by the motor. So the iron loss and the copper loss of the motor will cause the temperature rise. When the hydrostatic spindle works, the spindle rotates at the speed of 390 rpm, the inlet pressure is up to 11 MPa, and the designed oil film thickness is only 25 μm. So the viscous power dissipation of the hydraulic oil will be another main internal heat source. The heat taken away by the hydraulic oil will cause the temperature rise of the hydraulic oil in the oil tank. So the inlet temperature increases constantly with time. Meanwhile, the convective heat transfers between the outside surfaces of the system and the ambient air occur with the temperature differences between them.

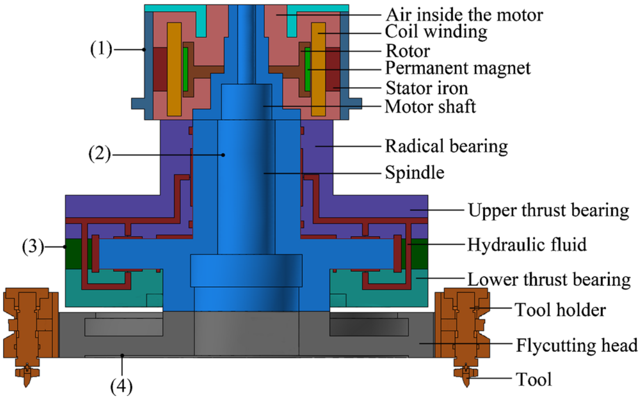

Fig. 1 Structure of the hydrostatic spindle system

In addition, thermal deformation occurs in the hydrostatic spindle system under the influence of the temperature field, which results in the change of the oil film thickness. Then the bearing load capacity will change accordingly with the oil film thickness, and the eccentricity of the bearing will also change under the influence of the external load and the self-gravity of the spindle. So the oil film thickness changes under the influence of thermal deformation and eccentricity. Meanwhile, the change of the oil film thickness also has an impact on the temperature field in return. Therefore, the interaction of thermal deformation, temperature field, and eccentricity exits during the operation of the hydrostatic spindle system.

Therefore, all the conditions mentioned above have to be considered in the simulation of the hydrostatic spindle system in order to improve accuracy. Therefore, the hydrostatic spindle system is modeled synthetically and the finite volume element method is proposed.

3 Model and FVEM

3.1 Heat-fluid–solid coupling model

The heat-fluid–solid coupling model is built based on the finite volume method. The heat generation process and the fluid–structure conjugate heat transfer are obtained by solving the energy equation in the following form [16]:

$$\frac{\partial}{\partial t}(\rho E)+\nabla\cdot\left(\vec{v}(\rho E+p)\right)=\nabla\cdot\left(k\nabla T+\left(\bar{\bar{\tau}}\cdot\vec{v}\right)\right)+S_{\mathrm{h}} \qquad (1)$$

where ρ is the density of the fluid or solid, E is the energy content per unit mass, $\vec{v}$ is the velocity vector, p is the pressure, k is the conductivity, T is the temperature, $\bar{\bar{\tau}}$ is the stress tensor, and S_{h} is any other volumetric heat source.

In Eq. (1), the term S_{h} represents the energy caused by the copper loss and iron loss of the motor, and the term $\nabla\cdot\left(\bar{\bar{\tau}}\cdot\vec{v}\right)$ represents the energy caused by the viscous power dissipation of the hydraulic oil. For the term $\nabla\cdot(k\nabla T)$, it is used to calculate the heat transfers among the solid, hydraulic fluid, and ambient air.

Meanwhile, the flow field is also obtained by the FVM. Because the hydraulic oil in the hydrostatic bearing is in the laminar flow regime and is assumed to be the steady viscous incompressible flow, the flow field is calculated by solving Eqs. (2) and (3):

$$\frac{\partial u}{\partial x}+\frac{\partial v}{\partial y}+\frac{\partial w}{\partial z}=0 \qquad (2)$$

$$\frac{\partial}{\partial t}\left(\rho\vec{v}\right)+\nabla\cdot\left(\rho\vec{v}\vec{v}\right)=-\nabla p+\nabla\cdot\left(\bar{\bar{\tau}}\right) \qquad (3)$$

where u, v, and w are the x, y, and z components of velocity $\vec{v}$, and $\bar{\bar{\tau}}$ is the stress tensor.

Therefore, the mathematical model of the heat-fluid–solid coupling analysis is composed of Eqs. (1), (2), and (3). Based on the mathematical model, the finite element model is built by the FLUENT software. In the finite element model, the hydraulic oil, the motor, and the hydrostatic spindle are all included. The inlet pressure (11 MPa) and the rotational speed (390 rpm) of the spindle are assigned to the finite element model. The heat generation rates are also assigned to the coil winding and the stator iron core of the motor in the model. In addition, the periodic boundary condition is adopted in the finite element model to raise the calculation speed.

3.2 Finite volume element method

As mentioned above, the oil film thickness is influenced by thermal deformation and eccentricity. So the oil film thickness can be obtained by Eq. (4):

$$h_{\mathrm{i}} = h_0 - \Delta h_{\mathrm{d}} - \Delta h_{\mathrm{e}} \tag{4}$$

where h_{i} is the oil film thickness when $t=t_{\mathrm{i}}$, h_0 is the initial oil film thickness, Δh_{d} is the change of the oil film thickness caused by the thermal deformation when $t=t_{\mathrm{i}}$, and Δh_{e} is the change of the oil film thickness caused by the eccentricity under the influence of the external load and self-weight of the spindle when $t=t_{\mathrm{i}}$.

So the FEM is used to calculate Δh_{d} in Eq. (4) by solving Eq. (5) [17]:

$$[K]\{\delta\} = P_{\mathrm{T}} \tag{5}$$

where $[K]$ is the stiffness matrix, $\{\delta\}$ is the displacement vector, and P_{T} is the temperature load.

For the radial bearing and the lower thrust bearing, Δh_{e} can be obtained by Eq. (6). However, Δh_{e} of the upper bearing is the opposite of the value obtained by Eq. (6):

$$\Delta h_{\mathrm{e}} = (W_0 - W_{\mathrm{d}})/J_{\mathrm{d}} \tag{6}$$

where W_0 is the load capacity of the bearing before thermal deformation, W_{d} is the load capacity of the bearing after the thermal deformation when $t=t_{\mathrm{i}}$, and J_{d} is the stiffness of the bearing after thermal deformation when $t=t_{\mathrm{i}}$.

For the thrust bearing, the parameter W_0 can be obtained by Eq. (7):

$$W_0 = G + f \tag{7}$$

where G is the self-gravity of the spindle and f is the external load in the z-axis direction exerted on the tool nose.

By solving Eqs. (2) and (3), the pressure field (p) of the hydraulic oil can be calculated when $t=t_{\mathrm{i}}$. Then the bearing load capacity (W_{d}) is obtained by integrating the fluid pressure. Based on the bearing load capacity (W_{d}), the stiffness (J_{d}) is obtained.

In order to consider the interaction among the temperature field, thermal deformation, and eccentricity, Eqs. (1)–(3) and (4) have to be coupled together. So the finite volume element method (FVEM) is proposed. Figure 2 shows the schema of the FVEM with structural parameters, material characteristics, and machining parameters as input and thermal error, machining accuracy, and machine tool performance as output. In Fig. 2, the power losses are denoted by the terms S_{h} and $\nabla\cdot\left(\overline{\overline{\tau}}\cdot\vec{v}\right)$ of Eq. (1). In the FVEM, the temperature field T obtained by Eq. (1) is adopted as the temperature load P_{T} in Eq. (5). Meanwhile, the thermal deformation $\{\delta\}$ obtained by Eq. (5) and the eccentricity obtained by Eqs. (2)–(3) and (6) are used to update the model, that is to update the parameters such as pressure p and velocity vector $\vec{v}$ in Eqs. (1)–(3). Therefore, the change of the oil film thickness will be fed back to the heat-fluid–solid coupling model constantly during the simulation in order to consider the interaction among the temperature field, thermal deformation, and eccentricity.

The proposed method is realized by combining the FLUENT software and the ANSYS software. The data transfer between them is done by the user-defined function (UDF) and the ANSYS parameter design language (APDL). The inlet temperature change of the hydraulic oil is measured by the experiment and is imposed on the model by the UDF.

Figure 3 shows the iteration process of the FVEM, which indicates that the proposed method is an iterative algorithm. The structure of the system is assumed to be changeless at every time interval Δt and is updated at discrete time points according to thermal deformation and eccentricity.

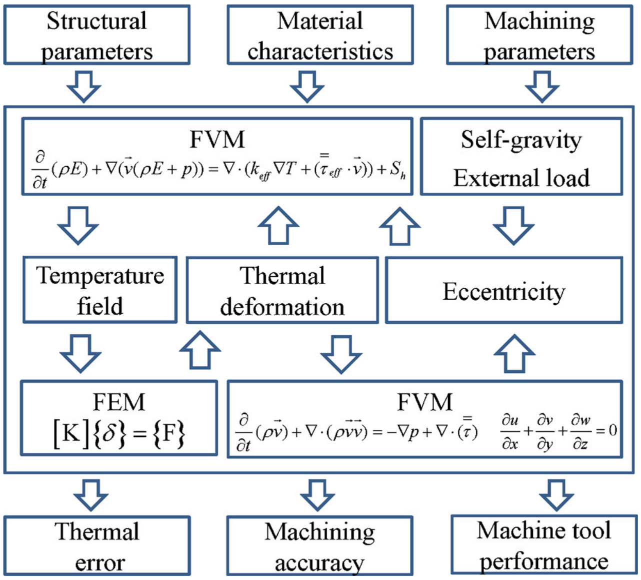

Fig. 2 Schema of the FVEM

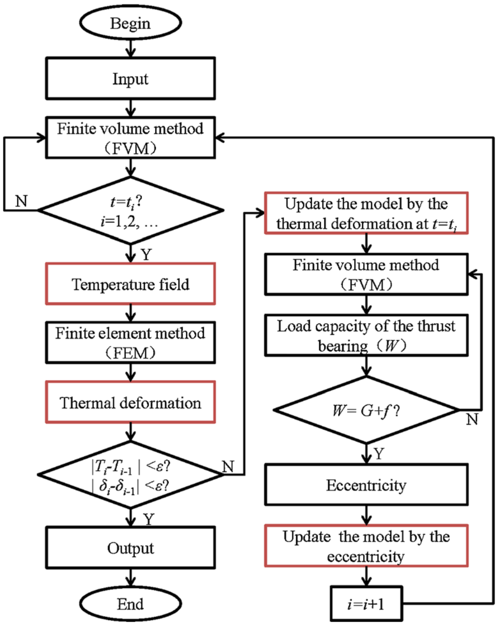

Fig. 3 Flow chart of the FVEM

The implementation process of the FVEM can be divided into four interrelated parts:

1. The calculation of the temperature field using the FLUENT software
2. The calculation of the thermal deformation using the ANSYS software
3. The updating of the model by thermal deformation using the UDF and the APDL
4. The updating of the model by eccentricity using the UDF and the APDL

In order to start the simulation according to Fig. 3, the heat sources are studied firstly.

4 Heat sources analysis

For the studied hydrostatic spindle system, the heat source consists of the motor, the hydraulic oil, and ambient air. The heat generation rates are assigned to the stator iron core and the coil winding to simulate the heat generation process of the motor. The heat generation process of the hydraulic oil is directly simulated by solving Eq. (1) using the FLUENT software. The influence of the ambient air is considered by imposing the convective heat transfer coefficients in all the outside surfaces of the system.

4.1 Heat generation rate of the motor

As shown in Fig. 1, the permanent magnet synchronous motor is used in the hydrostatic spindle system. So the eddy current loss of the rotor can be neglected because its magnetic field is almost constant. Therefore, the main heat sources in the motor are the iron loss and copper loss of the stator. Both the iron loss and the copper loss consist of two parts: intrinsic loss and additional loss. For the studied model, only the intrinsic loss is taken into consideration, which is the main heat source of the motor.

The heat generation rates caused by the iron loss and copper loss of the stator can be obtained respectively by [18]:

$$P = K_a P_{1.0/50} B^2 \left(\frac{f}{50}\right)^{1.3} \tag{8}$$

$$P_{Cu} = 3I^2 R \tag{9}$$

where P is the heat generation rate caused by the iron loss, P_{Cu} is the heat generation rate caused by the copper loss, $K_a=1.5$ is the correction factor, $P_{1.0/50}=4.7$ W/kg is the heat generation rate per unit weight when $f=50$ Hz and $B_{max}=1.0$ T, $B=0.8$ T is the air gap flux density, $f=39$ Hz is the alternative frequency, $I=4.7$ A is the phase current, and $R=1.68\ \Omega$ is the phase resistance.

The iron core is composed of 0.5-mm-thick silicon steel sheets, each of which is coated with the insulating medium which degrades the thermal conductivity of the iron core drastically. The coil winding is coated with the insulating varnish as well. Therefore, the equivalent thermal conductivities are introduced with consideration of the influence of the insulating medium and the insulating varnish, which are given by:

$$\lambda_T = 1 \Big/ \left(\frac{K_{Fe}}{\lambda_1} + \frac{1-K_{Fe}}{\lambda_0}\right) \tag{10}$$

$$\lambda_R = \left(\delta_{Cu} + \delta_j\right) \Big/ \left(\frac{\delta_{Cu}}{\lambda_{Cu}} + \frac{\delta_j}{\lambda_j}\right) \tag{11}$$

where λ_T is the equivalent thermal conductivity of the iron core, λ_R is the equivalent thermal conductivity of the coil winding, $K_{Fe}=0.95$ is the lamination factor, $\lambda_1=40$ W/(m °C)

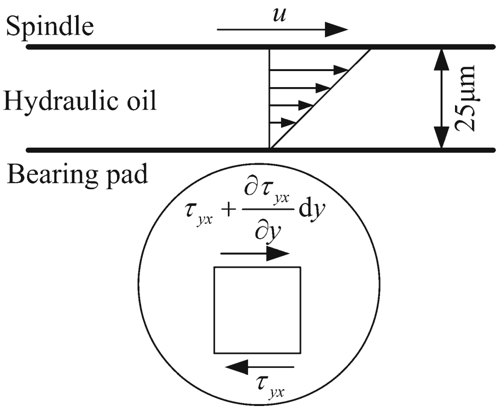

Fig. 4 Flow in the lands and the *x* direction shear stresses on a 2D element

is the thermal conductivity of the silicon steel, λ_0=0.2 W/(m °C) is the thermal conductivity of the insulating medium, δ_{Cu}= 0.53 mm is the diameter of the copper wire, δ_{j}=0.05 mm is the thickness of the insulating varnish, λ_{Cu}=387.6 W/(m °C) is the thermal conductivity of the copper, and λ_{j}=0.2 W/(m °C) is the thermal conductivity of the insulating varnish. According to Eqs. (8)–(11), P=20.6 W, P_{Cu}=111.3 W, λ_{T}=3.6 W/(m °C), and λ_{R}=4.39 W/(m °C).

4.2 Heat source in the hydrostatic bearing

Figure 4 shows the relative motion in the lands between the spindle and the bearing pads. The shear stresses in the x-axis direction on a two-dimensional (2D) element extracted from the hydraulic oil are also shown in Fig. 4.

From Fig. 4, it can be seen that the power of the element resulting from the shear stresses in the x-axis direction can be obtained by [16]:

$$p_x = \left(u\tau_{yx} + \frac{\partial(u\tau_{yx})}{\partial y}\mathrm{d}y - u\tau_{yx}\right)\mathrm{d}x = \frac{\partial(u\tau_{yx})}{\partial y}\mathrm{d}x\mathrm{d}y. \qquad (12)$$

Then for the three-dimensional (3D) element, the power of the element resulting from the viscous stresses can be obtained by:

$$\begin{aligned} p &= \nabla\cdot(\overline{\overline{\tau}}\cdot\vec{v})\mathrm{d}x\mathrm{d}y\mathrm{d}z \\ &= \left(\frac{\partial(u\tau_{xx})}{\partial x} + \frac{\partial(u\tau_{yx})}{\partial y} + \frac{\partial(u\tau_{zx})}{\partial z} + \frac{\partial(u\tau_{xy})}{\partial x} + \frac{\partial(u\tau_{yy})}{\partial y} + \frac{\partial(u\tau_{zy})}{\partial z} + \frac{\partial(u\tau_{xz})}{\partial x} + \frac{\partial(u\tau_{yz})}{\partial y} + \frac{\partial(u\tau_{zz})}{\partial z}\right)\mathrm{d}x\mathrm{d}y\mathrm{d}z \end{aligned} \qquad (13)$$

where τ_{ij} is the shear stress in the i-axis direction on the face perpendicular to the j-axis direction; τ_{xx}, τ_{yy}, and τ_{zz} are the normal stresses; and u, v, and w are the components of the velocity vector. The τ_{ij} is related to the viscosity and the velocity gradient of the hydraulic oil.

Because the velocity gradient varies with the position of the element, the heat generation rates in different positions of the hydraulic oil vary widely, and the temperature distribution of the hydraulic oil is asymmetrical. Therefore, it is inaccurate to simplify the heat source in the hydrostatic bearing to constant values (temperatures or heat generation rates). In the proposed FVEM, the temperature distribution is calculated by integrating Eq. (1) in each element using the FLUENT software so that the actual heat generation process is simulated and the more accurate temperature distribution is obtained.

4.3 Computation of the convection heat transfer coefficients

The heat convection between the outside surfaces of the spindle system and the ambient air occurs with differences in temperature between them. The heat transfer regimes (natural or forced convection) of the outside surfaces have to be determined before calculating the convection heat transfer coefficients. For the stationary surfaces such as surfaces (1) and (3) shown in Fig. 1, the heat transfer regime is the natural convection obviously. For the rotary surfaces, such as surfaces (2) and (4) shown in Fig. 1, the heat transfer regime is determined by [7]:

$$\frac{Gr}{Re^2} = \frac{g\beta L\Delta T}{(R\omega)^2} \qquad (14)$$

where Gr is the Grashof number, Re is the Reynolds number, g is the acceleration of gravity, β is the volumetric thermal expansion coefficient, ΔT is the temperature difference between the wall surface and ambient air, L is a characteristic scaling length of the wall geometry, R is the rotation radius, and ω is the rotation speed.

If $Gr/Re^2 >> 1$, the natural convection takes dominant position in the heat transfer, whereas if $Gr/Re^2 << 1$, the forced convection does. Based on Eq. (14), the heat transfer regimes of all outside surfaces are determined after assuming the temperature difference (ΔT) from experience for each wall surface. Then the convection heat transfer coefficient can be obtained by:

$$h = (Nu\lambda)/L \qquad (15)$$

where λ is the heat conductivity of the fluid, L is the characteristic scaling length of the wall geometry, and Nu is the Nusselt number.

For the natural convection, the Nusselt number is determined by the Grashof number and the Prandtl constant, which is given by [19]:

$$Nu = 0.59(Gr\cdot Pr)^{0.25}. \qquad (16)$$

For the forced convection, the Nusselt number is determined by the Reynolds number, which is given by [20]:

$$Nu = 0.326(Re)^{0.5} \quad 4 \le Re \le 200,000. \qquad (17)$$

Then the convection heat transfer coefficients of all wall surfaces are obtained. Table 1 only presents the calculation results of surfaces (1)–(4) shown in Fig. 1.

Table 1 Convection heat transfer coefficients of surfaces (1)–(4)

Type	Wall surface	L	ΔT	Pr or Re	Gr	Nu	h
Natural convection	(1)	0.13	9	0.71	2,850,000	22	4.6
	(3)	0.155	14	0.71	5,300,000	28	4.82
Forced convection	(2)	0.107	5	66,000	880,000	83.75	21
	(4)	0.07	10	6,800	490,000	26.9	10.3

5 Calculation results and analysis

5.1 Calculation results

Based on the heat source analysis, the thermal analysis is carried out by the FLUENT software and the initial temperature field when $t=5$ min is obtained as shown in Fig. 5. Based on the initial temperature field, thermal deformation when $t=5$ min is calculated by the ANSYS software as shown in Fig. 6. Then the oil film thickness under the influence of the thermal deformation is studied. Figure 7 shows the oil film thicknesses at the position of the bearing lands after the thermal deformation when $t=5$ min. The arc-shaped bearing lands are displayed in the cylindrical coordinate, so they are square-shaped in Fig. 7.

From Fig. 7a, it can be seen that the oil film thickness of the lower thrust bearing decreases along the radial direction. The oil film thicknesses at some positions of the lower thrust bearing land are less than the designed oil film thickness and the oil film thickness at other positions are greater than the designed oil film. As shown in Fig. 7c, the oil film thickness of the radial bearing decreases along the z-axis direction. However, the oil film thickness of the radial bearing decreases compared with the designed oil film thickness. Under the influence of the displacement constraints, the oil film thickness of the upper thrust bearing changes in a different way, as shown in Fig. 7b.

For the studied fly cutting machine tool, the external load f exerted on the tool nose is so small that its influence on the eccentricity of the radial bearing can be neglected. So only the influence of the forces in the z-axis direction on the eccentricity of the thrust bearing is considered. Then according to Eq. (15), $\Delta h_e=0.22$ μm when $t=5$ min is obtained.

Based on the thermal deformation and the eccentricity of the spindle obtained by the FEM and the FVM, respectively, the heat-fluid–solid model is updated by the UDF and the APDL. Then another loop computation is carried out based on the updated model. According to the proposed method, the working process of the hydrostatic spindle system within 3 h is simulated and the influence of the temperature field on the performance of the hydrostatic spindle system is studied.

5.2 Calculation results analysis

5.2.1 Variation of the oil film thickness

Based on the calculation results, the oil film thicknesses at different times are calculated by Eq. (4). To each bearing, the shapes of the oil film at any time are like that when $t=5$ min shown in Fig. 7. However, the changing amplitude of the oil film thickness increases over time. In order to study the variation of the oil film thickness with time, the oil film

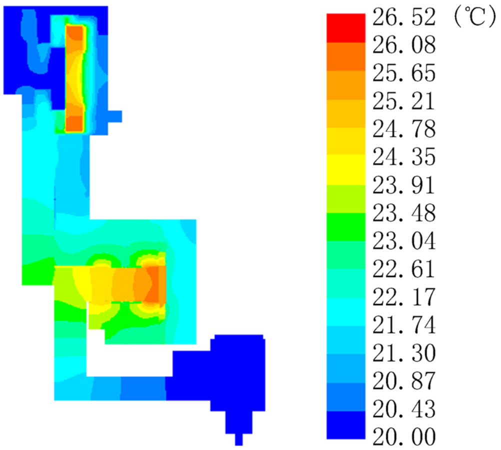

Fig. 5 Temperature field when $t=5$ min

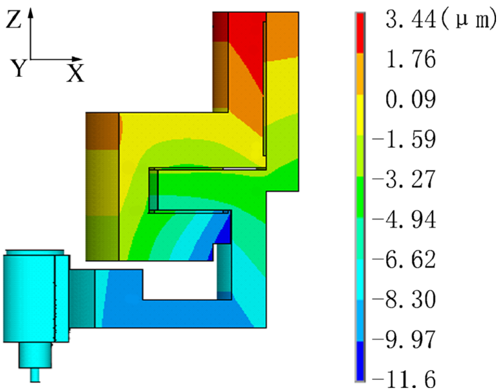

Fig. 6 Thermal deformation in z direction when $t=5$ min

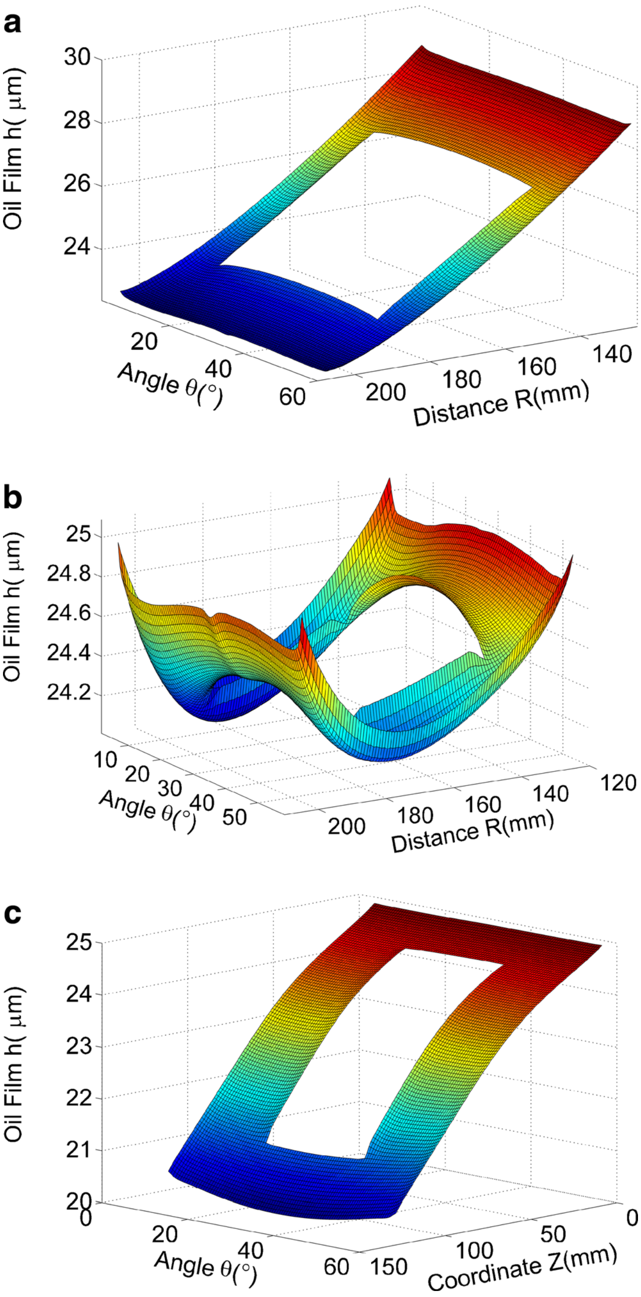

Fig. 7 Oil film thickness distribution. **a** The lower thrust bearing; **b** the upper thrust bearing; **c** the radial bearing

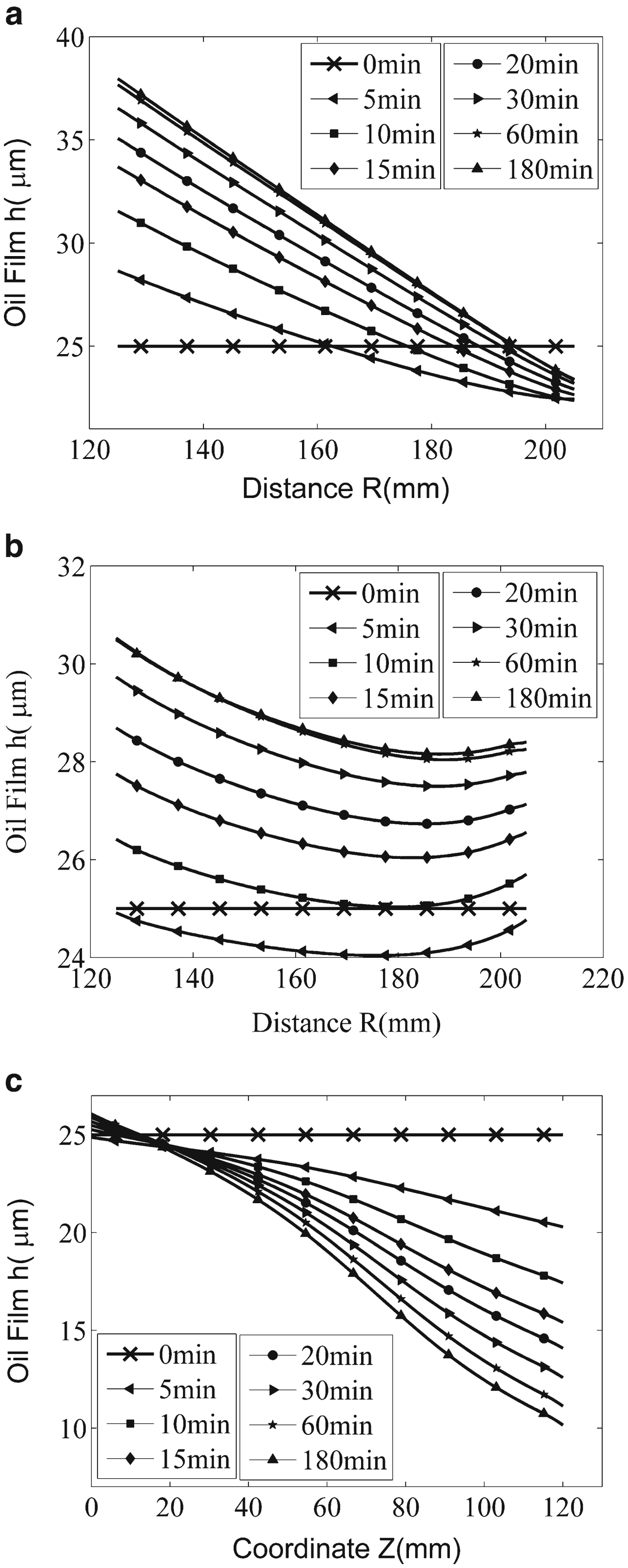

Fig. 8 Oil film thickness distribution at different times. **a** The lower thrust bearing when θ=3.5°; **b** the upper thrust bearing when θ=3.5°; **c** the radial bearing when θ=8.85°

thicknesses at different times in a certain position of each bearing land are extracted, as shown in Fig. 8.

From Fig. 8a–c, it can be seen that the oil films of the lower bearing and the radial bearing are wedge-shaped under the influence of the temperature rise, and the wedge angles increase monotonously over time. Compared with the designed oil film thickness (25 μm), the oil film thickness of the radial bearing decreases with time. For the lower thrust bearing, the region where the oil film thickness is less than 25 μm decreases with time. However, for the upper bearing, the variation of the oil film thickness with time is different with the others, as shown in Fig. 8b. The oil film thickness of the upper thrust bearing decreases firstly and increases subsequently compared with the designed oil film thickness. The difference is caused by the displacement constraint imposed on the upper bearing by the beam of the studied machine tool.

5.2.2 *Variation of the bearing load capacity*

Because the bearing load capacity is determined by the oil film thickness, the bearing load capacity will change with the oil film thickness. Figure 9 shows the variation of the bearing load capacity with time.

As shown in Fig. 9a, the load capacity of the radial bearing increases continuously with the oil film thickness until it becomes stable. Because the oil film thickness of the radial bearing decreases constantly as shown in Fig. 8c, its load capacity increases with time. From Fig. 9b, it can be seen that the load capacities of the lower thrust bearing and the upper thrust bearing increase slightly first, then decrease rapidly, and finally, tend to be stable. The variation of the upper thrust bearing's load capacity is consistent with the variation of its oil film thickness. For the lower thrust bearing, the oil film thickness in a large region decreases at the beginning, so its load capacity increases firstly.

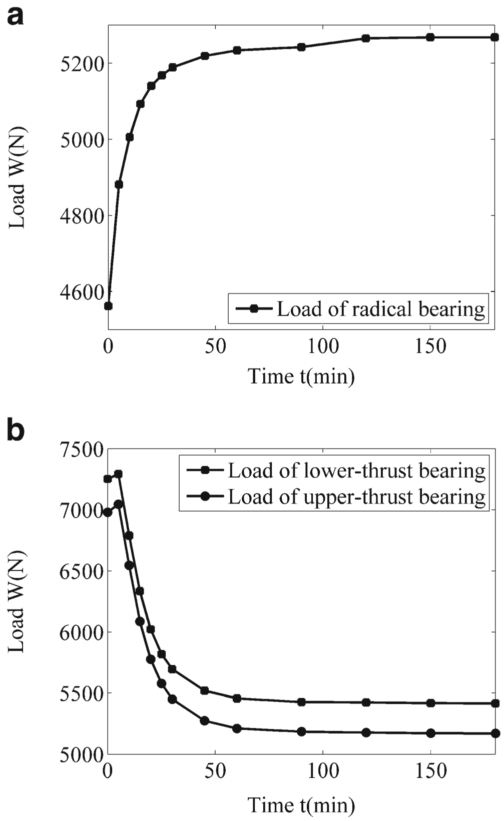

Fig. 9 Variation of the bearing load capacity. **a** The radial bearing; **b** the lower thrust bearing and the upper thrust bearing

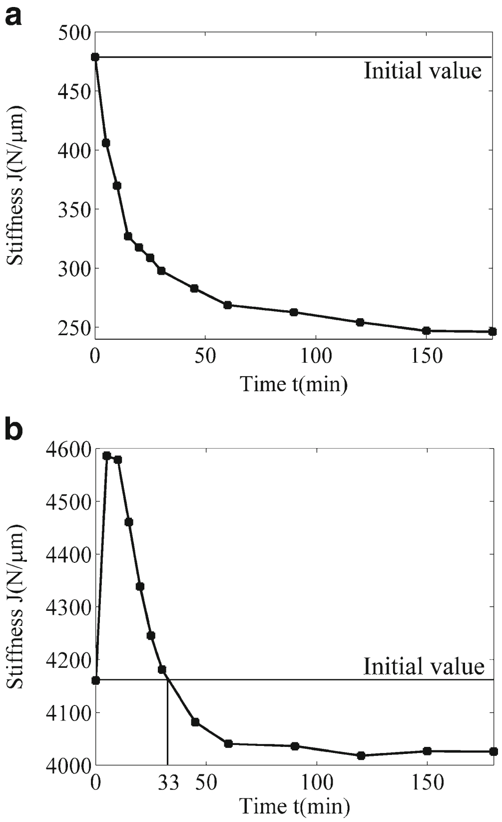

Fig. 10 Variation of the static stiffness. **a** The radial bearing; **b** the thrust bearing

5.2.3 *Variation of the static stiffness*

Under the influence of the oil film thickness, the static stiffness will also change with time, as shown in Fig. 10. As shown in Fig. 10a, the static stiffness of the radial bearing decreases rapidly, the initial value of which is 478.68 N/μm.

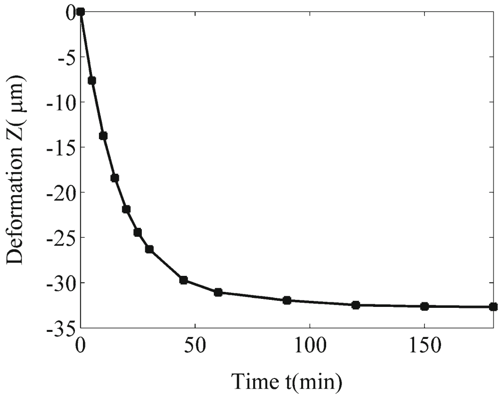

Fig. 11 Thermal displacement history of the tool nose

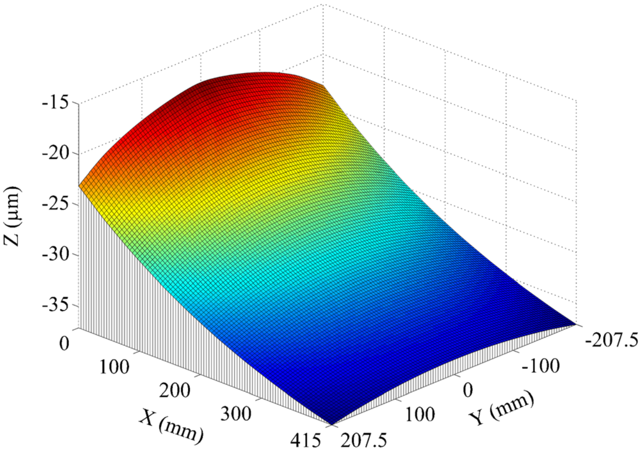

Fig. 12 Surface shape of the workpiece

The monotonous change of the radial bearing's static stiffness is determined by the variation of its oil film thickness. For the thrust bearing, the initial value of the static stiffness is 4,160.63 N/µm. As shown in Fig. 10b, the static stiffness of the thrust bearing increases firstly and then decreases. In the first 33 min, the static stiffness of the thrust bearing is higher than the initial value and the maximum value is up to 4,585.9 N/µm. From Fig. 10, it can be seen that the static stiffness of the radial bearing decreases by 232.38 N/µm (48.5 %) after 3 h and that the static stiffness of the trust bearing decreases by 142.63 N/µm (3.4 %) after 3 h under the influence of the temperature rise. Therefore, the influence of the temperature rise on the radial bearing is greater than that on the thrust bearing.

5.2.4 Influence of thermal displacement on machining precision

Considering the influence of the temperature field, the deformation of the tool nose in the *z* direction caused by thermal displacement and eccentricity is predicted by the proposed model and method, as shown in Fig. 11. From Fig. 11, it can be seen that the deformation of the tool nose in the *z* direction can reach above 30 µm, which will influence the surface precision of the workpiece directly. Then the influence of the deformation on the machining accuracy is studied.

The studied fly cutting machine tool is used to machine flat surfaces, as shown in Fig. 13. The feed of the workpiece is achieved by a horizontal axis slide. The feed speed of the slide and the cutting thickness are 300 µm/s and 10 µm, respectively. Then if the machining is processed on the workpiece when the machine tool starts for 5 min rather than when it reaches the thermal balance, the surface shape of the workpiece caused only by the temperature rise is predicted by the proposed model and method, as shown in Fig. 12.

From Fig. 12, it can be seen that the finished surface appears as a slope in the direction of the feed, that is in the *x*-axis direction, under the influence of the temperature rise. While in the *y*-axis direction, the finished workpiece is thicker in the middle than at both sides. In Fig. 12, the flatness error of

Fig. 13 Hydrostatic spindle system and experimental equipments. **a** Hydrostatic spindle system; **b** sensor system; **c** control system and SCADA

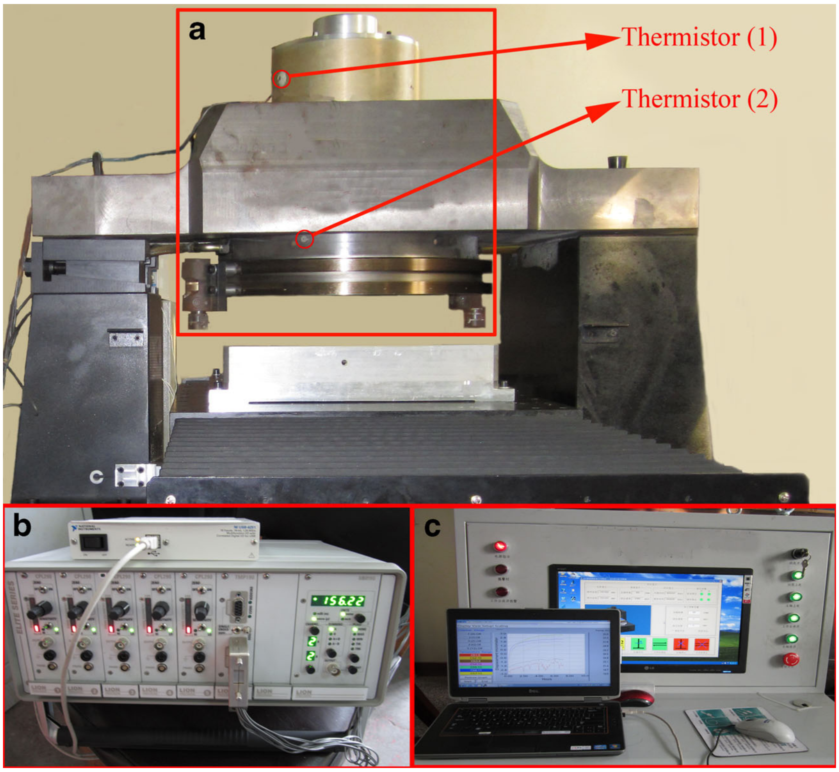

the finished surface is up to 18.6 μm. So the influence of the temperature rise on the flatness error of the workpiece is great, which has to be considered before the machining process. In order to reduce the influence of the thermal displacement on the machining accuracy, the machining process should be started after the machine tool has reached thermal balance.

6 Experiment verification

Because the hydrostatic spindle rotates at high speed, it is difficult to measure the thermal displacement of the tool nose. Meanwhile, the surface shape of the workpiece is determined by the comprehensive performance of the machine tool, so the surface shape of the workpiece cannot be used to validate the proposed model and method. Therefore, the proposed heat-fluid–solid coupling model and the FVEM are validated by measuring the temperature variation of the spindle system. The experimental setup is shown in Fig. 13. The sensor system (TM190) is used to process the signals. Meanwhile, the supervisory control and data acquisition (SCADA) is realized by using a laptop. Thermistors (1) and (2) are used to obtain the temperature variations of the motor casing and the outside surface of the thrust bearing, respectively.

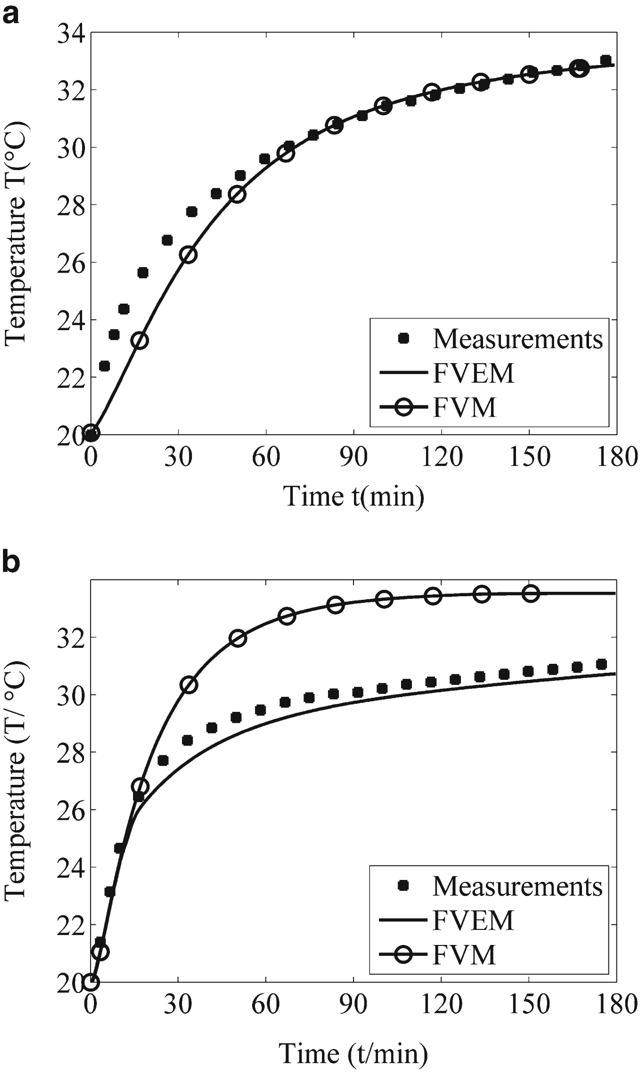

Fig. 14 Comparison of temperature histories. **a** Location (1); **b** location (2)

Panels a and b of Fig. 14 are comparisons between the measured and simulated temperature histories of two locations. The temperature variations using the FVM are obtained without consideration of the interaction among the temperature rise, thermal deformation, and eccentricity.

From Fig. 14a, it can be seen that the temperature variations of the motor casing obtained by the FVEM and the FVM are the same, which agree with the measured values well within 3 h. So the influence of the thermal deformation on the temperature rise of the motor can be neglected. For the thrust bearing, the temperature variation obtained by the FVEM is more consistent with the experimental data than that obtained by the FVM, as shown in Fig. 14b. Under the influence of thermal deformation, the oil film thickness of the thrust bearing increases so that the heat caused by the viscous power dissipation decreases. So the temperature obtained by the FVM is higher than that obtained by the FVEM. By comparison, the proposed heat-fluid–solid model and method are validated.

7 Conclusions

In order to study the influence of the temperature rise on the hydrostatic spindle system, the integrated heat-fluid–solid coupling model was built and the finite volume element method (FVEM) was proposed.

1. The heat generation process and the fluid–structure conjugate heat transfer of the hydrostatic spindle system were simulated directly by the proposed heat-fluid–solid coupling model using the FLUENT software, which improved the simulation precision.
2. Based on the heat-fluid–solid coupling model and the finite volume element method, the two-way heat-fluid–solid coupling analysis was made on the hydrostatic spindle system with consideration of the interaction among the temperature rise, thermal deformation, and eccentricity. Then the temperature field, thermal deformation, and eccentricity at different times were obtained.
3. Based on the calculation results, the variations of the oil film thicknesses were studied considering the influence of thermal deformation and eccentricity. Then the influence of temperature rise on the load capacity, the static stiffness, and the machining accuracy was studied.
4. The experiment was set up to validate the proposed model and the finite volume element method. The temperature histories calculated by the proposed model and the FVEM agreed well with the experimental data.

Acknowledgments The project is supported by the National Science Fund for Distinguished Young Scholars of China [grant number 50925521].

References

1. Bryan J (1990) International status of thermal error research. CIRP Ann 39(2):645–656
2. Weck M, Mckeown P, Bonse R, Herbst U (1995) Reduction and compensation of thermal errors in machine tools. CIRP Ann 44(2): 89–598
3. Liang RJ, Ye WH, Zhang HH, Yang QF (2013) The thermal error optimization models for CNC machine tools. Int J Adv Manuf Technol 63:1167–1176
4. Hsieh KH, Chen TR, Chang P, Tang CH (2013) Thermal growth measurement and compensation for integrated spindles. Int J Adv Manuf Technol 64:889–901
5. Creighton E, Honegger A, Tulsian A, Mukhopadhyay D (2010) Analysis of thermal errors in a high-speed micro-milling spindle. Int J Mach Tools Manuf 50(4):386–393
6. Kim JJ, Jeong YH, Cho DW (2004) Thermal behavior of a machine tool equipped with linear motors. Int J Mach Tools Manuf 44(7–8): 749–758
7. Chen DJ, Bonis M, Zhang FH, Dong S (2011) Thermal error of a hydrostatic spindle. Precis Eng 35(3):512–520
8. Zhao HT, Yang JG, Shen JH (2007) Simulation of thermal behavior of a CNC machine tool spindle. Int J Mach Tools Manuf 47:1003–1010
9. Zhang JF, Feng PF, Chen C, Yu DW, Wu ZJ (2013) A method for thermal performance modeling and simulation of machine tools. Int J Adv Manuf Technol 68:1517–1527
10. Mayr J, Weikert S, Wegener K (2007) Comparing the thermo-mechanical behavior of machine tool frame designs using a FDM-FEM simulation approach. Proceedings ASPE annual meeting:17–20
11. Mayr J, Ess M, Weikert S, Wegener K (2009) Compensation of thermal effects on machine tools using a FDEM simulation approach. Proceedings Lamdamap, vol.9. ISBN 1861941188
12. Jedrzejewski J, Kowai Z, Kwasny W, Modrzycki W (2004) Hybrid model of high speed machining centre headstock. CIRP Ann 53(1): 285–288
13. Holkup T, Cao H, Kolář P, Altintas Y, Zelený Y (2010) Thermo-mechanical model of spindles. CIRP Ann 59(1):365–368
14. Li DX, Feng PF, Zhang JF, Wu ZJ, Yu DW (2014) Calculation method of convective heat transfer coefficients for thermal simulation of a spindle system based on RBF neural network. Int J Adv Manuf Technol. doi:10.1007/s00170-013-5386-y
15. Mayr J, Jedrzejewski J, Uhlmann E, Donmez MA, Hartig F, Wendt K, Morwaki T, Shore P, Schmitt R, Brecher C, Wurz T, Wegener K (2012) Thermal issues in machine tools. CIRP Ann 61:771–791
16. Anderson JD (1995) Computational fluid dynamics: the basics with applications. McGraw Hill, New York
17. Larson MG, Bengzon F (2013) The finite element method: theory, implementation and applications. Springer, Heidelberg
18. Zhang HL (2010) Iron Losses and transient temperature field of permanent magnetic synchronous motor, Dissertation, Harbin institute of technology
19. Wu TH, Wang XM, G.L. Xu GL (2011) Engineering thermodynamics. Huazhong University of Science and Technology Press, Wuhan
20. Cardone G, Astarita T, Carlomagno GM (1997) Heat transfer measurements on a rotating disk. Int J Rotating Mach 3:1–9